Real-time Microdamage and Strain Detection during Micromechanical Testing of Single Trabeculae

R. Jungmann, G. Schitter, G. E. Fantner, M. E. Lauer, P. K. Hansma, and P. J. Thurner
Physics Department, University of California, Santa Barbara, CA 93106, USA

ABSTRACT
Research in bone diseases like osteoporosis is motivated by its immense social impact and health care costs. While there are numerous studies about the influence of bone mineral density and microarchitectural properties on the mechanical properties of trabecular bone, little is known about the influence of bone matrix material properties. In this communication, we present novel ways for combining mechanical testing of single trabeculae with imaging on both the micro- and nanoscale to further investigate these material properties. Our results indicate microdamage in an ellipsoid zone on the tension side of the trabeculae tested in three-point bending. We estimated the highest tensile strains in this region to be about 3.5%. Quantitatively global whitening versus distance curves correlate well with retrieved force-distance data. Scanning electron microscopy investigations of the microdamaged and optically whitened zones suggest that damage formation happens primarily in the bone and not on the surface. In addition to whitening/microdamage assessment on the microscale, we used atomic force microscopy together with a custom made three-point bending device and a region based digital image correlation tool to obtain quantitative local surface displacements on the bending side of single trabeculae. We found that bone deformation is heterogeneous with different surface domains shearing off each other. The two novel methods presented make it possible to investigate the dynamics of plasticity and failure of bone both on the micro- and on the nanoscale.

Keywords: Trabecular Bone, Fracture, High-Speed Photography, Stress-Whitening, Microdamage, Three-Point Bending, Atomic Force Microscopy, Digital Image Correlation, Strain Detection.

INTRODUCTION

Bone is a tissue extensively studied using histology [1], mechanical testing [2], micro-computed tomography [3, 4], magnetic resonance imaging [5], ultrasound [6], nanoindentation and Atomic Force Microscopy (AFM) [7]. Most of bone research is motivated by the immense social impact in health care due to osteoporosis in post-menopausal women and the aged [8, 9] as well as the enormous medical costs (13.8 billion US$ in the USA alone in 1995). Osteoporosis results in bone loss and change of trabecular architecture and tissue composition, causing a decrease in bone strength. It is generally accepted nowadays that besides bone density also bone microarchitecture and bone matrix material properties, a combination referred to as bone quality, are also important factors influencing fracture resistance. Thus the accurate diagnosis of bone fracture resistance based solely on bone density proves to be difficult. Therefore the diagnosis of bone fracture risk should also include other parameters of bone quality. Whereas there exist numerous studies on the microarchitecture of trabecular bone and how these could be exploited for fracture risk diagnosis [10-12], there are almost no studies addressing the bone matrix material properties of trabecular bone. This is despite the fact that bone composition does change with age and disease [13, 14]. Even if changes in composition are subtle, they can still have huge effect on the mechanical properties of the bulk tissue. Presumably only a small fraction of noncollagenous proteins in bone tissue guides and controls the assembly of the major components as collagen type I fibrils, about 100 nm in diameter and up to 10 µm and more in length, as well as carbonated hydroxyapatite ($Ca_{10}(PO_4)_6(OH)_2$) crystals with typical sizes of 50 nm x 25 nm x 3 nm [15-17]. With the presented study we demonstrate novel ways for combining mechanical testing of single trabeculae with imaging on both the micro- and nanoscale. With these tools it is possible to investigate the dynamics of plasticity and failure of bone in a qualitative and quantitative fashion. Our results show the correlation of whitening to microdamage and to tensile strains. In addition we can estimate the tensile strains involved in microdamage formation in the presented loading case. First nanoscale imaging results of bone plasticity allow us to indicate bone failure mechanisms like sliding of collagen fibrils as proposed by Gupta et al. [18].

MATERIALS AND METHODS

Sample Preparation

Proximal parts of bovine femora were obtained from a local grocery store (Gelson's Market, Santa Barbara, CA, USA). Single trabeculae were either tested directly after preparation or stored at -20 °C after preparation until testing. For preparation femoral bones were first cut in half along the long axis of the bone. The halves were then cut perpendicular to the long axis into slabs of ~5 cm in thickness using a butcher's band saw. Bone marrow was subsequently extracted from the specimen using a jet of pressurized water. A pair of scissors was used to extract samples with similar rod-like shapes, which were mostly found in the regions closer to the diaphysis. A total of 12 single trabeculae were excised for mechanical testing, 10 of which were imaged with high-speed photography whereas 2 were imaged with AFM. The dimensions of the ten samples imaged with high-speed photography were measured using a pair of calipers. The average length was determined to be (2.52 ± 0.21) mm and the mean diameter to be (0.56 ± 0.14) mm.

Mechanical Testing with High-Speed Photography Imaging

For three-point bending testing of single trabeculae and imaging with high-speed photography, we used a custom-made mechanical testing device previously described in detail [19, 20]. The system, which was initially made for compression testing of mm-sized, cuboid trabecular bone samples, was modified for three-point bending tests of single trabeculae. A u-shaped jig (cp. Figure 1 A) was put in the sample chamber providing the two lower points of support. The third point of support was facilitated through changing from a previously flat to a triangulated plunger, which exerted the displacement on the sample roughly in the middle between the two lower points of support. Further the signal from the load cell (Model LBC-100, Transducer Techniques Inc., Temecula, CA, USA was amplified by a factor of 10 using an analog amplifier (LPF-100B, Warner Instruments Corp., Hamden, CT, USA) to provide sufficient signal to noise ratio. All samples were tested immersed in a buffer containing 150 mM NaCl and 10 mM Hepes, at pH 7.0. The mechanical tests consisted of two phases: in the first phase the piston was lowered slowly until a preloading force of 0.6 N was reached, in order to find the sample top. In the second phase the sample was loaded at a constant displacement rate of up to 600 µm displacement, at a displacement rate of 600 µm/s. For imaging we used an Ultima 512 high-speed camera (Photron Inc., San Diego, CA, USA) equipped with a KC, a KC-AUX, and an IF-3 lens (Infinity, Boulder, CO, USA). The samples were illuminated from the front using two fiber lights (MH-100, Dolan Jenner Industries Inc., Lawrence, MA, USA) at horizontal angles of about ±45°. All videos were recorded with a frame rate of 60 frames/s and a shutter speed of 1/12000 s.

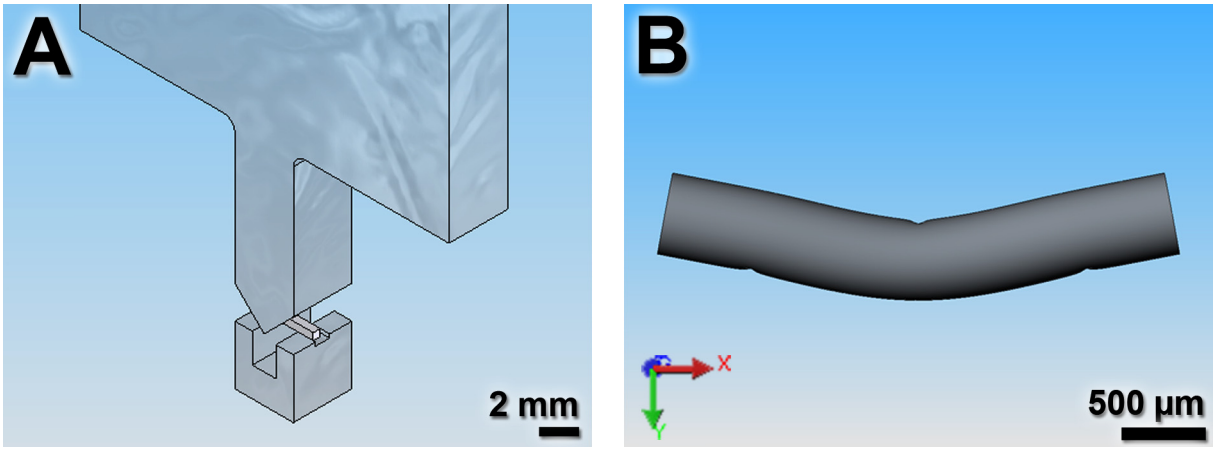

Figure 1: Illustration of the three-point bending test setup consisting of a triangular shaped plunger and a u-shaped jig holding a single trabecula in place **(A)**. Finite element illustration of specimen deformation after exerting a plunger displacement of 350 µm in y-direction **(B)**.

Mechanical Data Analysis

In order to calculate the elastic modulus and strain at the tension side from a typical force-distance curve experimentally obtained (cp. Figure 5), the trabecula is regarded as an Euler-Bernoulli (Equation (1)). The geometry of the specimens is assumed to a beam of length L and radius R. The out-of-plane displacement w of a beam is governed by the Euler-Bernoulli beam equation:

$$\frac{d^2}{dx^2}\left[EI\frac{d^2w}{dx^2}\right] = p \qquad (1)$$

where p is the distributed loading (force per unit length) acting in the same direction as y (and w), E is the Young's modulus of the beam, and I is the area moment of inertia of the beam's cross section. If E and I do not vary with x along the length of the beam, then the beam equation simplifies to

$$EI\frac{d^4w}{dx^4} = p \tag{2}$$

For three-point bending tests of animal bone [21], the following equations are obtained for the highest tensile strain and the elastic modulus, assuming a circular cross section of the specimen ($I = \pi R^4/4$):

$$\varepsilon = 12 \cdot \frac{d_{\max} \cdot c}{L^2} \quad \text{(Tensile Strain)} \tag{3}$$

$$d_{\max} = \frac{FL^3}{48 \cdot EI} = \frac{4 \cdot FL^3}{48 \cdot E\pi R^4} \quad \text{(Elastic Modulus)}$$
$$\Rightarrow E = \frac{FL^3}{12 \cdot d_{\max}\pi R^4} \tag{4}$$

, with the parameters ε : strain, $d_{\max}$: maximum displacement on the sample perpendicular to its long axis , c : distance to neutral fiber, L : sample length, E : apparent elastic modulus, F : load on specimen and R : radius of cross section.

The elastic modulus was retrieved from recorded force-distance curves by fitting a straight line to the most linear portion of the curve and using equation (4). The yield point was also determined from this fit; it is defined by the intersection of the force-distance curve with a straight line having 90% slope and the same origin as the previously fitted line. The failure point was defined as the global maximum in the force-distance curve.

High-Speed Photography Image Processing

Whitening of bone, due to microdamage, was quantified using a thresholding algorithm as previously described [19]. In brief, a threshold for whitening was determined from the histograms of five consecutive frames prior to compression, which accounted for the approximate period of intensity flickering of the fiber lights. From the five histograms the highest average pixel value was calculated and subsequently used as a threshold, i.e. all pixels having a higher value were counted as whitened pixels in each frame. Due to flickering of the fiber lights, the raw whitening curve exhibited a considerable amount of noise, which was smoothed by applying a median filter (rank 100). 150 frames (or more), before the beginning and after the end of the relevant frames showing sample compression, were included in the filtering process in order to suppress artifacts at the start and the end of the filtered curves. For the synchronization of whitening values with recorded load-distance curves a standard DIC algorithm [22] was applied. A high contrast region on the plunger was manually selected and tracked through consecutive frames. Synchronization was achieved by correlating the detected total movement of the plunger in y-direction (i.e. the loading direction) in pixels to the total displacement measured by the mechanical testing device.

Scanning Electron Microscopy (SEM)

After mechanical testing, some of the bone samples were rinsed with water to remove residual buffer, air-dried in a furnace at 37 °C over night, and then fixed with conducting paint to a custom-made aluminum sample holder allowing for sample rotation. The sample holder facilitated SEM imaging of the samples from the side, i.e. aligned with the high-speed photographs, as well as from the bottom, where the highest tension is expected. Subsequently the samples were sputtercoated (Desk II, Denton Vacuum, Moorestown, NJ, USA) with a ~5 nm thick gold layer. Finally the samples were imaged using an SEM (Vega TS 5130MM, Tescan Brno, Czech republic), with an acceleration voltage of 20 keV.

Mechanical Testing with AFM Imaging

AFM measurements were conducted using a Dimension 3100 AFM and a Nanoscope IIA controller (Veeco Inc., Santa Barbara, CA, USA) mounted on a vibration isolation table (Nanoscience Instruments, Phoenix, USA). For contact mode imaging, rather soft cantilevers (MLCT-AUHW, Veeco Inc.) were used. For tapping mode imaging cantilevers with a nominal spring constant of 40 N/m and a resonance frequency of 300 kHz (RTESPW, Veeco Inc.) were used. The design of the three-point bending device for the AFM (see Figure 2) was similar to the geometry of the setup used in combination with high-speed photography setup, but was flipped upside down (cp. Figure 2). Since we were interested in the tension side, the displacement was exerted by the part with the two outer support points in the upper frame instead of moving the middle one. This approach also keeps the surface of the bent trabecula within the vertical positioning range of the AFM scanner for imaging.

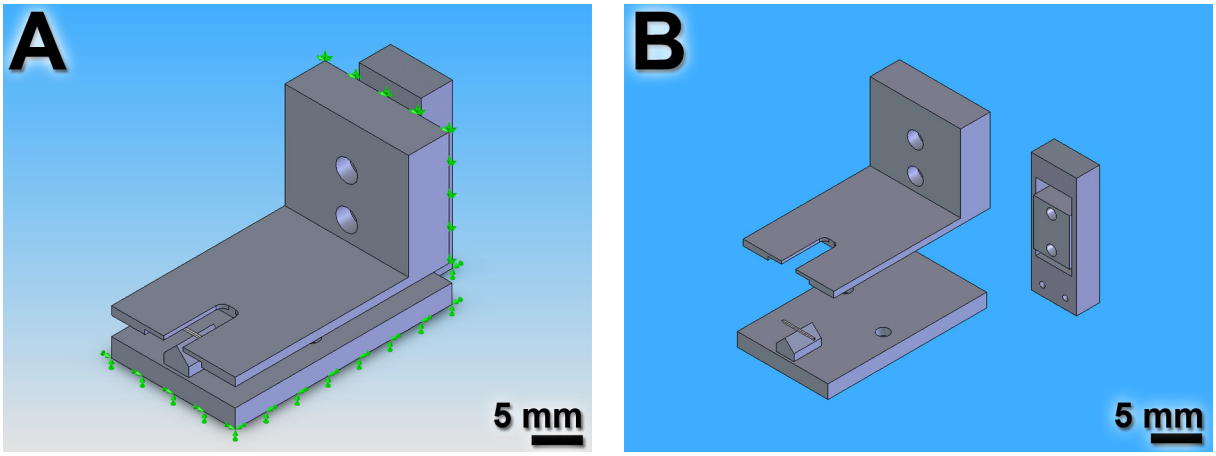

Figure 2: CAD model of the three-point bending device with displacement control through a 1D linear stage and a force sensor (not visible in the image) underneath the plunger in the middle **(A)**. Exploded view of the different device parts including the bone specimen placed on the plunger **(B)**.

The design (cp. Figure 2 and Figure 3) also includes a capacitive force sensor (Flexiforce, Tekscan, South Boston, MA, USA) glued in between the middle support-point and the ground plate with 2-ton epoxy (ITW Devcon, Danvers, MA, USA). The base plate is screwed to a linear motion stage (MS-125-X, Newport, Irvine, CA, USA) and to the sample stage of the AFM. The frame exerting the displacement is mounted to the linear motion stage. It has a 5 mm wide and 8 mm deep cutout in the front, providing the two moved support points for three-point bending (cp. Figure 2). The linear motion stage is driven by an 80 tpi screw, i.e. is translated 317.5 µm per turn.

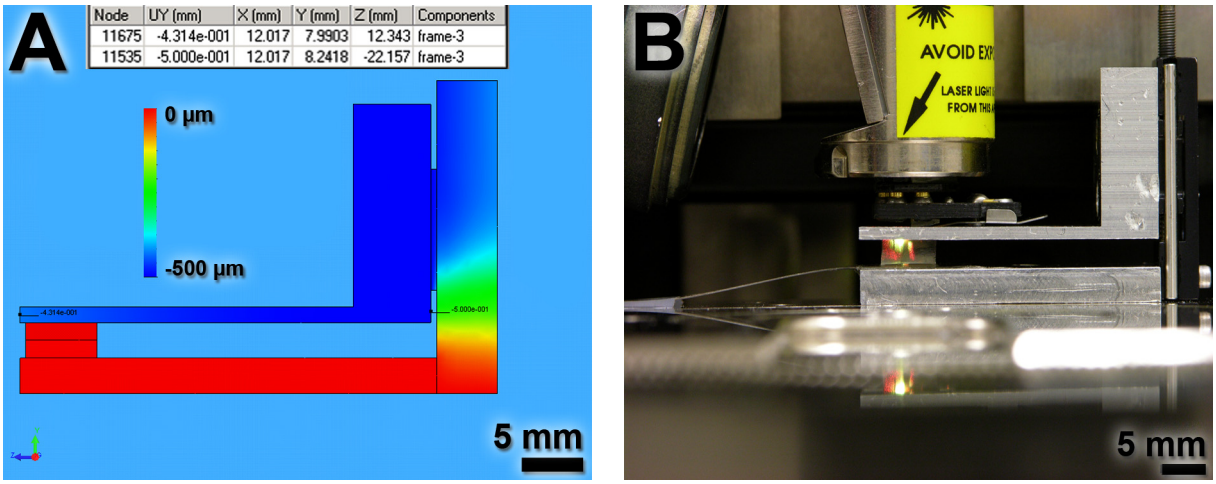

Figure 3: Finite element analysis of the three-point bending device made of aluminium after a 500 µm displacement in y-direction of the linear stage with the bone specimen in testing place **(A)**. FEA shows the need of optical displacement detection for the stage. Setup of the device under the D3100 AFM together with the thin flexiforce force sensor underneath the middle plunger **(B)**.

A finite element simulation (cp. Figure 3 A) predicted a resulting displacement at the point of the bone specimen of about 431 µm when the stage was moved 500 µm assuming a tested trabecula with a diameter of 0.3 mm and an isotropic elastic modulus of 2 GPa. This means an error of 69 µm or 13.8% making a distance measurement through counting of screw turns rather inaccurate. Therefore displacement of the bending device was detected using photographs from a digital still camera (Coolpix 8700, Nikon Corporation, Tokyo, Japan) placed in front of the AFM setup (cp. Figure 3 B). A picture was captured before and after exerting the bending displacement. Then the DIC algorithm described in the high-speed photography section was used to determine the displacement of the upper frame by calculating a differential displacement through the position of the frame and the plate. The differential measurement allowed reduction of the errors induced by accidental movement of the camera or setup between the two captured frames. The nominal optical resolution of this method is 20.5 µm/px resulting in a resolution of around 2 µm (through subpixel accuracy of the DIC algorithm) for the displacement measurement, which is sufficient for our purpose. Since we used an open-loop AFM scanner, all AFM images of the trabeculae

have been captured with a 90° scan angle such that the long axis of the trabecula was parallel to the fast scan axis (x-axis) in order to reduce artifacts due to scanner drift. In addition only frames that were recorded in the same direction of the slow scan axis (up or down) were correlated to reduce the influence of nonlinearities such as hysteresis. Position offsets were not applied to the scan, because they were previously reported to induce nonlinear scan behavior [23]. In all cases images comprising a scan area of 20 µm were captured at 0.5 lines/s. During bending experiments first an image of an undeformed sample was acquired, then the AFM cantilever was withdrawn, the specimen was bent, the tip re-engaged to the same position and the same sample area was imaged again.

AFM Image Processing

All AFM images were in a first step processed using the Nanoscope software (Version 7.00R2.sr2, Veeco Inc.). Height images were processed using a 1st order *planefit* and a 0th order *flattening* command, whereas amplitude or deflection images were processed using only a 1st order *planefit.* The surface displacement measurements for consecutive AFM images were conducted using a regional interrogation-window-based particle-image-velocimetry algorithm [24]. Dividing the image in 16x16 px large quadratic interrogation windows and allowing 50% overlap from one image to the next was adequate. For the actual correlation calculation, a freeware module (MatPIV, [25]) for MATLAB (The MathWorks, Natick, MA, USA) was used. From the obtained displacement information, we calculated the local strain in the direction parallel to the long axis of the trabecula (fast scan axis), by computing the gradient in this direction: $\varepsilon_x = du/dx$. For validation purposes we also scanned a calibration grating with 5 µm pitch size (Veeco Inc.) and subjected the retrieved data to the surface displacement measurement.

RESULTS

Mechanical Testing with High-Speed Photography

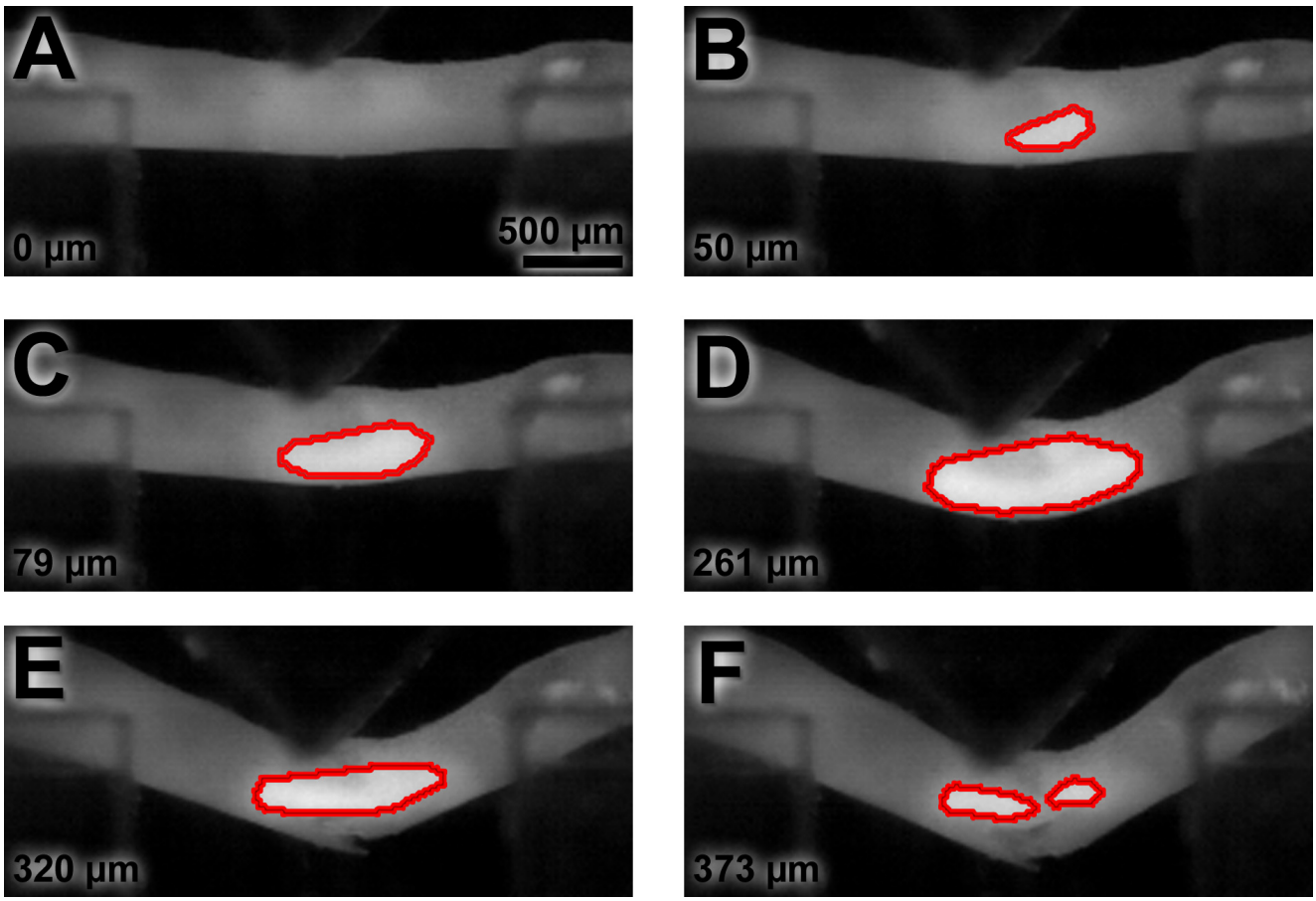

Figure 4: Single trabecula from femoral bovine bone at different displacements during a three-point bending test. The red contour shows the detected whitened area, due to microdamage. After failure, the whitened region follows the propagating crack tip **(E, F)**.

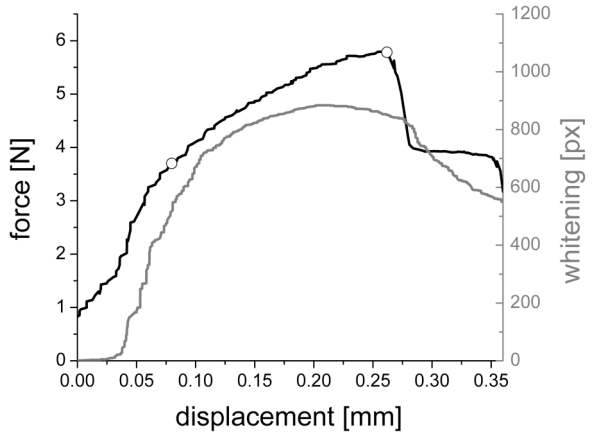

Figure 5: Detected whitening (gray) and force exerted on the sample (black) versus displacement of the trabecula shown in Figure 4. The two open circles in the force curve denote the yield point (first) and failure point (second), respectively.

A typical result of a three-point bending experiment is shown in Figure 4; starting at 50 µm displacement we detected whitening, developing on the tensile side of the specimen (red contours marked in Figure 4 B-F). The whitening starts prior to the yield point (at 79 µm displacement) and rises in the region of plastic deformation. As soon as a macroscopic crack develops, i.e. at the failure point at 261µm displacement (cp. Figure 4 E, F), the whitening fades in the lower regions of the sample and follows the propagating crack tip. The correlation between force and whitening can be seen in Figure 5. An estimation of the tensile strain at the bottom of the single trabecula (denoting the fiber with highest tensile strain) using the sample displacement and Euler-Bernoulli beam equation (cp. equation (3)) leads to a tensile strain of 3.5% at the point where the whitening starts (at 50 µm displacement). The presented mechanical and whitening behavior is representative for a total of 10 investigated samples. The apparent elastic modulus of the tested sample was calculated using Equation (4) to 1.24 GPa and lies well within in the range of the whole group (1.89 ± 0.91 GPa) and values previously reported [26] for single bone trabeculae. In order to assess microdamage in whitened areas of these single trabeculae, we prepared two samples for SEM imaging. Figure 6 shows a comparison of high-speed photography images and corresponding SEM images of two trabeculae after testing. One sample was bent beyond the failure point whereas the other one was unloaded after whitening had been observed. The propagating crack developed in the first sample (Figure **6** A) can clearly be seen in the SEM image (Figure 6 B). The SEM image of the uncracked sample (cp. Figure 6 D) shows no evident microcracks on the surface. However, we observed microcracks with uncracked ligament bridging when looking at an osteocytic lacuna as shown in Figure 6 D.

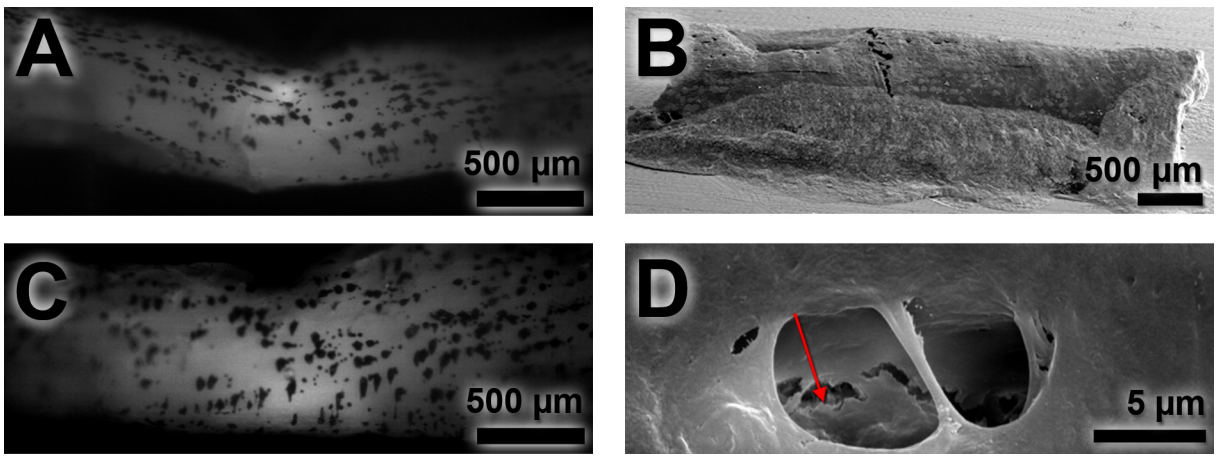

Figure 6: High-speed photography frame **(A)** together with SE micrograph **(B)** of a fractured single trabecula after three-point bending. HSP movie frame from a whitened but no fractured trabecula **(C)** and corresponding SE micrograph **(D)** showing microcracks developing in the bulk with crack bridging (red arrow). The black spots on the samples **(A, C)** are ink marks used for local strain computation (not shown).

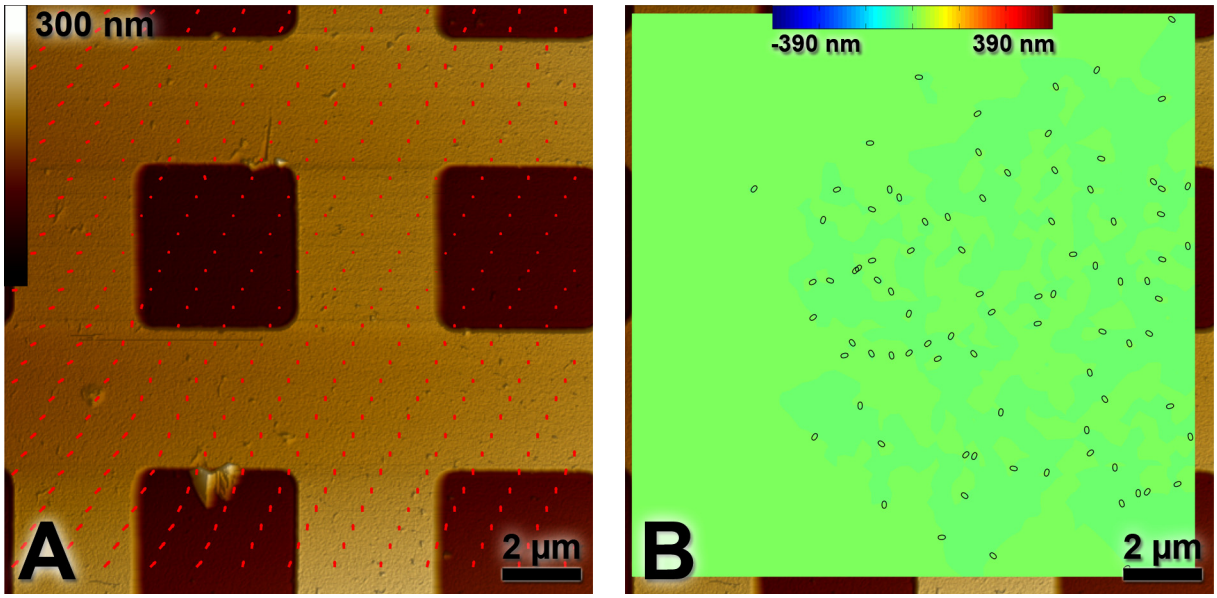

Figure 7: Zero deformation test using a 20 µm image of a calibration grating. The vector field exhibits almost no displacement (**A**, imaged in tapping mode, 0.5 Hz). The displacement field in x-direction (fast scanning axis) is a measure for the stability of the system **(B)**. The displacement distribution is almost uniform and the calculated average strain is 0.002 ± 0.001. (Image resolution is 512x512 px).

To validate the surface displacement measurements and to assess the drift of the piezo-driven open-loop scanner we first imaged a calibration grating with 5 µm pitch without applying deformation. The grating was imaged and frames were acquired continuously. Two consecutive frames captured with the same settings and in the same imaging direction were correlated using the surface displacement algorithm mentioned above. Figure 7 A and B show the resulting displacement vector field and the contour map in x-direction laid over the mixed height and amplitude image of the sample. The strain component in x-direction, $\varepsilon_x = du/dx$ was calculated to be 0.002 ± 0.001, thus on order of magnitude below the strains expected at the onset of plastic deformation.

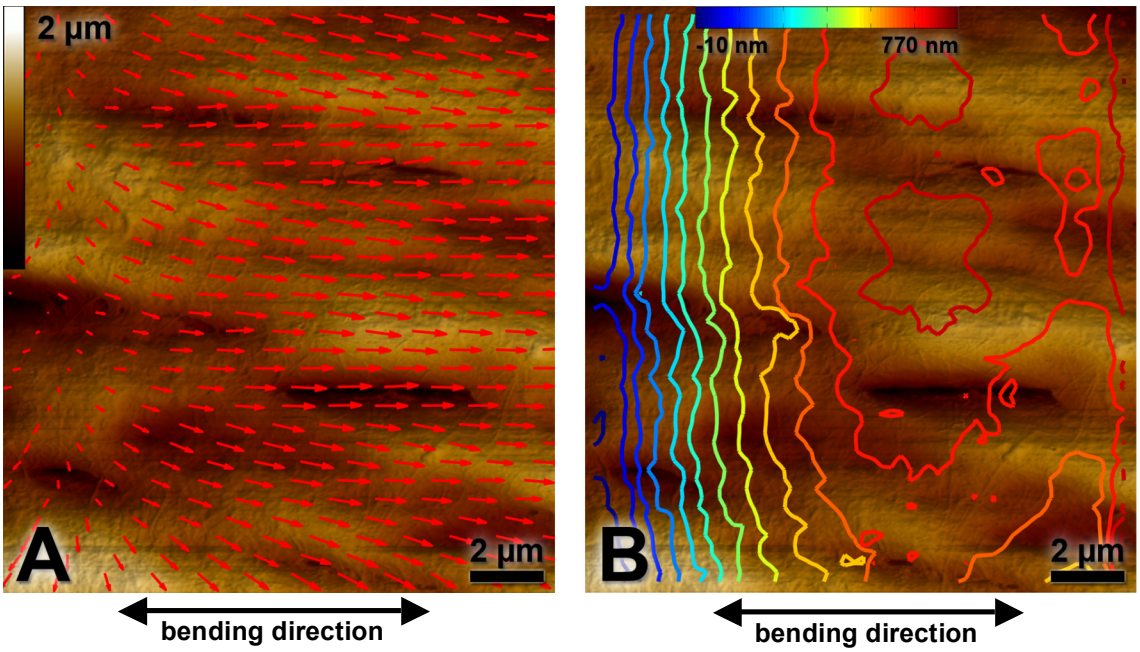

Figure 8: Mixed height and deflection AFM image of a single trabecula with overlay of the displacement field **(A)** and relative displacement in x-direction (fast scanning axis and bending direction) **(B)**. The image was obtained on a wet trabecula in contact mode (0.5 Hz). (Image resolution is 512x512 px).

In a first bending experiment, a single trabecula was imaged in wet condition. The sample was kept hydrated by connecting the ends of two tissues (Kimberly-Clark, Neenah, WI, USA) to the bone specimen and their other ends to a bath of de-ionized water. A 20 µm region on the surface was imaged, then the sample was bent and the same region was imaged again. The overlapping region of both images was matched using cross correlation techniques to make a perfect overlay at the most left part and both images were cropped to the overlapping region. Figure 8 A and B show the results of this bending experiment, evaluated with the surface displacement algorithm. Figure 8 A reveals neighboring domains bounded by several cavities where the displacement vectors point in different directions. Figure 8 B represents the surface displacement map in the bending direction (which is also the fast scanning axis). We calculated the average strain *du/dx* in this bending direction to be 0.021 ± 0.008.
In another experiment, we investigated another single trabecula bent in dry condition. Again a 20 µm region on the surface of the sample was imaged in air, then the sample was bent to a displacement of 99 µm and a force of 1.9 N and the same region was imaged again. Similarly as before, the images were matched to find their overall displacement. Figure 9 A and Figure 9 B show the results of that bending experiment, evaluated with the surface displacement algorithm. The white arrows in Figure 9 A show a collagen fiber bundle spanning from the top left corner almost diagonal over the image. Figure 9 B represents the surface displacement contour map in the bending direction (x-axis and fast scanning axis). We calculated the average strain *du/dx* in the bending direction to be 0.024 ± 0.006.

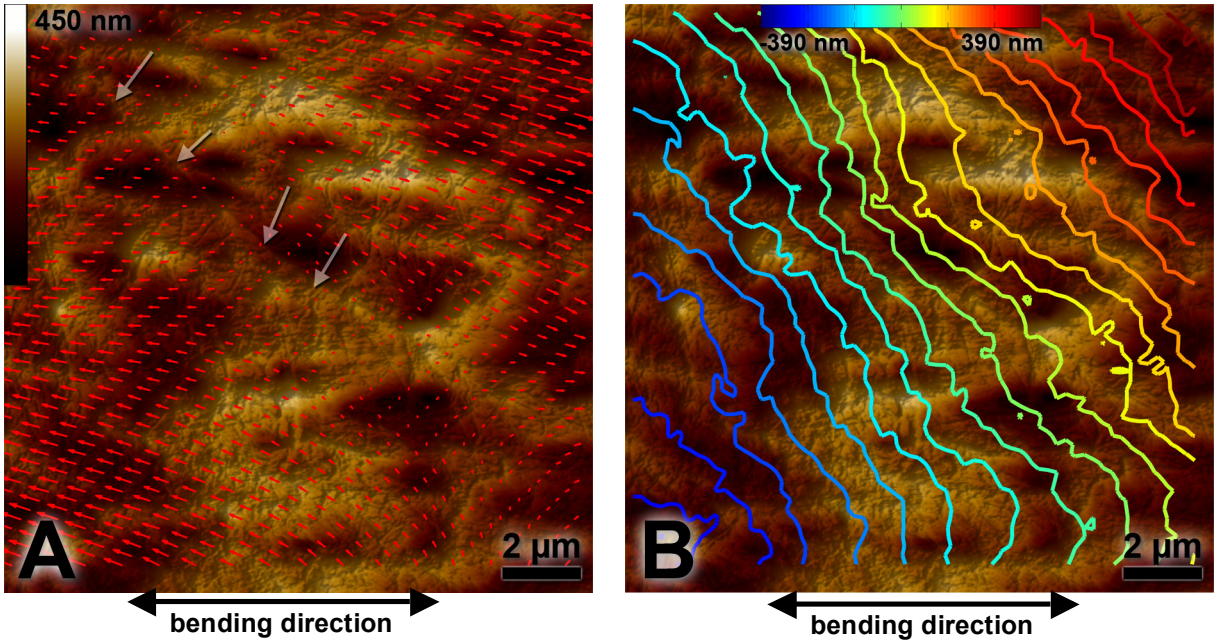

Figure 9: AFM mixed height and deflection image of a dry single trabecula with an overlay of the displacement field evaluated using the surface displacement algorithm **(A)**, image obtained in air using tapping mode (0.5 Hz). Same surface with a contour plot overlay of regions with same relative displacement in x-direction (fast scanning axis and bending direction) **(B)**. (Image resolution is 512x512 px).

DISCUSSION

High-speed photography combined with whitening detection is a tool for real-time detection of microdamage and failure in bone [19, 20]. Here we present an adapted experimental setup allowing testing of single trabeculae in a three-point bending geometry. Compared to earlier investigations [19, 20] of cuboid trabecular bone sample this approach has several advantages. Firstly, the geometry of single trabeculae from bovine femora is rod-like and thus very simple compared to complicated 3D structures of larger samples. Secondly, since we are using a 2D imaging approach, the rod-like shape allows us to assume axial symmetry of the sample. Thus it is reasonable to assume that what is observed is representative also for the backside of the sample. Thirdly, the simple geometry allows for a qualitative correlation between whitening and local strains and allows an estimation of quantitative strain values on the outermost layer of the sample using the Euler-Bernoulli equation.
Our results allow us the important insight that the whitening in this loading case correlates with areas of tensile strain as can be seen in Figure 4. Quantitatively it correlates well with the retrieved force-distance data. The SEM investigations of the whitened trabeculae indicate that microcracks in trabecular bone initially may develop below the softer osteoid surface of the bone. At least we could not find any microcracks on the surface of the sample that was loaded to whitening and unloaded prior to failure. Importantly we can, however, also in this case

correlate whitening to microcracks and microdamage, similar as previously reported [19, 20]. Using the Euler-Bernoulli equation we can estimate the highest tensile strains of the outermost fiber of the beam at the onset of whitening to a value of about 3.5%. Bone is a complicated composite material also exhibiting a mechanically non-linear behavior. Therefore the use of linear mechanics would lead to inaccurate results especially in the post-yield deformation regime. In order to assess effects of plasticity and local displacements and strains also beyond the elastic regime and correlate them with whitening and thus microcracks and microdamage, more sophisticated experimental and computational methods are needed. This could be done for example with an optical displacement detection method on the sample surface. Such development would also nicely complement efforts in finite element analysis of trabecular bone structures by providing a damage model with solid experimental foundation [27-31].

The results obtained from single trabeculae three-point bending tests using in-situ AFM so far gave helpful insights to the failure mechanism of bone on the nanoscale in a qualitative and quantitative fashion. AFM offers the necessary spatial resolution to visualize effects of plasticity and failure on the nanoscale. A similar investigation was previously reported from cortical bone using SEM as the imaging modality [32]. Experiments on the nanoscale were conducted at tensile surfaces strains of about 2%, very close to the strain of 3.5%, estimated to be sufficient for plastic deformation. The image results from the bending experiments shown in Figure 8 and 9 seem to support the proposed nanoscale failure mechanism in bone, as proposed by Gupta et al. in [18]. Their in-situ tensile test using synchrotron X-ray scattering revealed that bone deformation is not homogenous but distributed between a tensile deformation of the fibrils and a shearing in the interfibrillar matrix. Our experiments on the nanoscale appear to support this hypothesis. Different domains of the bone surface are sheared against each other along a bundle of collagen fibers under tensile stress (cp. Figure 9 A). This collagen fiber bundle is a clear boundary for areas that are displaced in opposite directions. However, experiments are difficult, when samples are wet or immersed in water or buffer. Due to adhesion forces between surface water films and the AFM tip, we could not yet find an experimental protocol that consistently works for wet samples. The situation is even more difficult for sample fully immersed in liquid due to the thermal drift of the sample-tip system, which also influences deformation measurement. In order to improve experimental imaging condition, we envision scanning in a closed fluid cell providing imaging in an environment close to saturated humidity in order to avoid sample drying. This could greatly improve image stability and reduce large amounts of water on the sample surface as sometimes encountered in wet samples. On the scanner side more sophisticated experimental and mathematical methods could virtually eliminate AFM scanner drifts as described in [33, 34]. Even better, however, would be the use of an AFM system with closed loop operation capability, leading to more accurate results in the slow scanning axis. Closed loop systems incorporating also feedback loops for the x- and y-direction, result in virtually no drifts due to piezo-scanner nonlinearities. Another option would be the use of a high-speed AFM system [35, 36]. Besides the fact, that drift would not be a great issue in such a system, it would even make it possible to observe dynamic effects of plasticity and failure in real-time, since samples could be tested dynamically instead of the stepwise deformation applied so far.

In conclusion, we present novel ways to assess effects of plasticity on both the micro- and the nanoscale. The simple geometry of the three-point bending tests allowed us not only to point out the correlation between whitening, i.e. microdamage, and tensile strains but also provided us with an estimate of the tensile strain needed for its creation. In addition AFM images gave insight into mechanisms of plastic deformation on the nanoscale. From our preliminary results we can approve a previously formulated damage model on this scale. Sure further advances on both micro- and nanoscale will provide us with more insight into bone failure in the future and allow observing the behaviour of the nanocomposite bone under load in-situ and in a dynamic fashion at the molecular level.

ACKNOWLEDGEMENTS

This work was supported by National Institutes of Health under Award R01 GM065354, by the NASA University Research, Engineering and Technology Institute on Bio-inspired Materials under Award No. NCC-1-02037 and by a research agreement with Veeco #SB030071. RJ acknowledges DAAD scholarship No. D/05/42569. GS acknowledges TU Delft, faculty 3mE grant PAL615. PJT acknowledges SNF Postdoctoral fellowship PA002-111445.

REFERENCES

1. Boyde, A. and V.J. Kingsmill, *Age changes in bone.* Gerodontology, 1998. **15**(1): p. 25-34.
2. Keaveny, T.M., E.F. Wachtel, C.M. Ford, and W.C. Hayes, *Differences between the Tensile and Compressive Strengths of Bovine Tibial Trabecular Bone Depend on Modulus.* Journal of Biomechanics, 1994. **27**(9): p. 1137-1146.

3. Feldkamp, L.A., S.A. Goldstein, A.M. Parfitt, G. Jesion, and M. Kleerekoper, *The direct examination of three-dimensional bone architecture in vitro by computed tomography.* J Bone Miner Res, 1989. **4**(1): p. 3-11.
4. Ruegsegger, P., B. Koller, and R. Muller, *A microtomographic system for the nondestructive evaluation of bone architecture.* Calcif Tissue Int, 1996. **58**(1): p. 24-9.
5. Wehrli, F.W., P.K. Saha, B.R. Gomberg, H.K. Song, P.J. Snyder, M. Benito, A. Wright, and R. Weening, *Role of magnetic resonance for assessing structure and function of trabecular bone.* Top Magn Reson Imaging, 2002. **13**(5): p. 335-55.
6. Rho, J.Y., *An ultrasonic method for measuring the elastic properties of human tibial cortical and cancellous bone.* Ultrasonics, 1996. **34**(8): p. 777-83.
7. Knapp, H.F., G.C. Reilly, A. Stemmer, P. Niederer, and M.L. Knothe Tate, *Development of preparation methods for and insights obtained from atomic force microscopy of fluid spaces in cortical bone.* Scanning, 2002. **24**(1): p. 25-33.
8. Cooper, C., E.J. Atkinson, S.J. Jacobsen, W.M. O'Fallon, and L.J. Melton, 3rd, *Population-based study of survival after osteoporotic fractures.* Am J Epidemiol, 1993. **137**(9): p. 1001-5.
9. Ray, N.F., J.K. Chan, M. Thamer, and L.J. Melton, 3rd, *Medical expenditures for the treatment of osteoporotic fractures in the United States in 1995: report from the National Osteoporosis Foundation.* J Bone Miner Res, 1997. **12**(1): p. 24-35.
10. Carballido-Gamio, J. and S. Majumdar, *Clinical utility of microarchitecture measurements of trabecular bone.* Curr Osteoporos Rep, 2006. **4**(2): p. 64-70.
11. Ladinsky, G.A. and F.W. Wehrli, *Noninvasive assessment of bone microarchitecture by MRI.* Curr Osteoporos Rep, 2006. **4**(4): p. 140-7.
12. Ulrich, D., T. Hildebrand, B. Van Rietbergen, R. Muller, and P. Ruegsegger, *The quality of trabecular bone evaluated with micro-computed tomography, FEA and mechanical testing.* Stud Health Technol Inform, 1997. **40**: p. 97-112.
13. Grynpas, M.D., J.H. Tupy, and J. Sodek, *The Distribution of Soluble, Mineral-Bound, and Matrix-Bound Proteins in Osteoporotic and Normal Bones.* Bone, 1994. **15**(5): p. 505-513.
14. McCreadie, B.R., M.D. Morris, T.C. Chen, D. Sudhaker Rao, W.F. Finney, E. Widjaja, and S.A. Goldstein, *Bone tissue compositional differences in women with and without osteoporotic fracture.* Bone, 2006. **39**(6): p. 1190-5.
15. Weiner, S. and W. Traub, *Bone structure: from angstroms to microns.* Faseb J, 1992. **6**(3): p. 879-85.
16. Eppell, S.J., W. Tong, J.L. Katz, L. Kuhn, and M.J. Glimcher, *Shape and size of isolated bone mineralites measured using atomic force microscopy.* J Orthop Res, 2001. **19**(6): p. 1027-34.
17. Kindt, J.H., P.J. Thurner, M.E. Lauer, B.L. Bosma, G. Schitter, G.E. Fantner, M. Izumi, J.C. Weaver, D.E. Morse, and P.K. Hansma, *In situ observation of fluoride-ion-induced hydroxyapatite-collegen detachment on bone fracture surfaces by atomic force microscopy.* Nanotechnology, 2007. **18**(13): p. 135102 (8pp).
18. Gupta, H.S., W. Wagermaier, G.A. Zickler, D.R.B. Aroush, S.S. Funari, P. Roschger, H.D. Wagner, and P. Fratzl, *Nanoscale deformation mechanisms in bone.* Nano Letters, 2005. **5**(10): p. 2108-2111.
19. Thurner, P.J., B. Erickson, R. Jungmann, Z. Schriock, J.C. Weaver, G.E. Fantner, G. Schitter, D.E. Morse, and P.K. Hansma, *High-Speed Photography of Compressed Human Trabecular Bone Correlates Whitening to Microscopic Damage.* Engineering Fracture Mechanics, 2007. **in press**(doi:10.1016/j.engfracmech.2006.05.024).
20. Thurner, P.J., B. Erickson, Z. Schriock, J. Langan, J. Scott, M. Zhao, J.C. Weaver, G.E. Fantner, P. Turner, J.H. Kindt, G. Schitter, D.E. Morse, and P.K. Hansma, *High-Speed Photography of the Development of Microdamage in Trabecular Bone during Compression.* Journal of Materials Research, 2006. **21**(5): p. 1093-1100.
21. *Shear and Three-Point Bending Test of Animal Bone.* ASABE Standard, 2001.
22. *IMAQ Vision Concepts Manual*, in *NI Vision*. 2005, National Instruments: Austin.
23. Jin, H. and H.A. Bruck, *A new method for characterizing nonlinearity in scanning probe microscopes using digital image correlation.* Nanotechnology, 2005. **16**(9): p. 1849-1855.
24. Markus Raffel, C.W., J. Kompenhans, *Particle Image Velocimetry - A Practical Guide*. 1998, New York: Springer.
25. Sveen, J.K., *An introduction to MatPIV v.1.6.1.* eprint series Dept. of Math. University of Oslo "Mechanics and Applied Mathematics", 2004(2).
26. Lucchinetti, E., D. Thomann, and G. Danuser, *Micromechanical testing of bone trabeculae - potentials and limitations.* Journal of Materials Science, 2000. **35**(24): p. 6057-6064.

27. Williams, J.L. and J.L. Lewis, *Properties and an anisotropic model of cancellous bone from the proximal tibial epiphysis.* J Biomech Eng, 1982. **104**(1): p. 50-6.
28. Dagan, D., M. Be'ery, and A. Gefen, *Single-trabecula building block for large-scale finite element models of cancellous bone.* Med Biol Eng Comput, 2004. **42**(4): p. 549-56.
29. Nagaraja, S., T.L. Couse, and R.E. Guldberg, *Trabecular bone microdamage and microstructural stresses under uniaxial compression.* Journal of Biomechanics, 2005. **38**(4): p. 707-716.
30. Shefelbine, S.J., U. Simon, L. Claes, A. Gold, Y. Gabet, I. Bab, R. Muller, and P. Augat, *Prediction of fracture callus mechanical properties using micro-CT images and voxel-based finite element analysis.* Bone, 2005. **36**(3): p. 480-488.
31. van Lenthe, G.H., M. Stauber, and R. Muller, *Specimen-specific beam models for fast and accurate prediction of human trabecular bone mechanical properties.* Bone, 2006.
32. Nicolella, D.P., A.E. Nicholls, J. Lankford, and D.T. Davy, *Machine vision photogrammetry: a technique for measurement of microstructural strain in cortical bone.* J Biomech, 2001. **34**(1): p. 135-9.
33. Croft, D., G. Shed, and S. Devasia, *Creep, hysteresis, and vibration compensation for piezoactuators: Atomic force microscopy application.* Journal of Dynamic Systems Measurement and Control-Transactions of the Asme, 2001. **123**(1): p. 35-43.
34. Sun, Y.F. and J.H.L. Pang, *AFM image reconstruction for deformation measurements by digital image correlation.* Nanotechnology, 2006. **17**(4): p. 933-939.
35. Fantner, G.E., G. Schitter, J.H. Kindt, T. Ivanov, K. Ivanova, R. Patel, N. Holten-Andersen, J. Adams, P.J. Thurner, I.W. Rangelow, and P.K. Hansma, *Components for high speed atomic force microscopy.* Ultramicroscopy, 2006. **106**(8-9): p. 881-887.
36. Schitter, G., G.E. Fantner, J.H. Kindt, P.J. Thurner, and P.K. Hansma. *On Recent Developments for High-Speed Atomic Force Microscopy*. in *IEEE/ASMEI International Conference on Advanced Intelligent Mechatronics*. 2005. Monterey, California, USA: IEEE.